Activation volume details from nonlinear anelastic deformation of a metallic glass

T. J. Lei, and M. Atzmon ⬚

View Online   Export Citation   CrossMark

Activation volume details from nonlinear anelastic deformation of a metallic glass

T. J. Lei[1] and M. Atzmon[1,2,a)] (iD)

AFFILIATIONS

[1]Department of Materials Science and Engineering, University of Michigan, Ann Arbor, Michigan 48109, USA
[2]Department of Nuclear Engineering and Radiological Sciences, University of Michigan, Ann Arbor, Michigan 48109, USA

[a)]Author to whom correspondence should be addressed: atzmon@umich.edu

ABSTRACT

At high stress, the viscosity of a metallic glass is non-Newtonian, and therefore the rate of anelastic stress relaxation is not linear in the applied stress. In this regime, one can obtain information on the details of the activation volume that are not accessible in the linear regime. While bending in the nonlinear regime introduces a complicated stress state, it offers great stability for noninstrumented measurements over many orders of magnitude of time. We have developed a method of controlled sample bending to a strain of up to ~0.0155 for $Al_{86.8}Ni_{3.7}Y_{9.5}$ metallic glass. Significant nonlinearity of the anelastic strain in the stress was observed, which is mainly associated with the largest and slowest shear transformation zones involved not reaching mechanical equilibrium at the end of the constraining period. Combining nonlinear kinetics under constraint and zero bending moment after constraint removal, the volume of the largest shear transformation zones and the transformation shear strain were obtained independently for the inherent state—their most likely values are $4.8 \times 10^{-28} \, m^3$ and 0.18, respectively.

I. INTRODUCTION

Metallic glasses (MGs) have drawn considerable attention due to their high strength and elastic limit.[1] However, they experience flow localization resulting in little macroscopic plasticity,[2] which limits their structural application. Understanding the deformation mechanism of MGs is necessary to identify ways to improve their plasticity. Unlike for crystalline alloys, knowledge of the microscopic origin of plastic deformation of MGs is incomplete due to their disordered structure. Physical analogs[3,4] have shown that macroscopic deformation is accommodated by cooperative shearing of atomic clusters, termed shear transformation zones (STZs).[5–8]

Plastic deformation of metallic glasses involves a large volume fraction of STZs in an activated flow state, for which STZ interactions are complex. In contrast, at small strain, the STZ volume fraction is small, in the dilute limit, so they are isolated. They can be reversed upon removal of external stress due to back stress in the elastic matrix, which leads to anelastic behavior.[9] In crystalline metals, several mechanisms of anelastic relaxation have been studied. We consider the STZ mechanism to dominate anelasticity in metallic glasses, based on the following points:

(a) The Snoek effect of small interstitial solutes[10] is unlikely in a metallic glass in the absence of, e.g., hydrogen or carbon atoms. (b) Chemical order-disorder effects,[11] if any, are weak in amorphous metals. (c) Any local jumps of constituent atoms are likely to be STZ mediated. (d) The present experiments involve a single phase and isothermal conditions.[11]

Anelastic deformation in the small-strain regime offers an opportunity to understand plasticity. Ju *et al.*[12] performed quasi-static anelastic relaxation measurements of $Al_{86.8}Ni_{3.7}Y_{9.5}$ (at. %) over a time range spanning seven orders of magnitude. The corresponding relaxation-time spectra were computed, which exhibited distinct peaks, representing an atomically quantized hierarchy of STZs, consisting of 14–21 atoms for the kinetic window observed. The measurements involved small anelastic strain and correspondingly small STZ volume fraction, 1%–2%.[12,13] Linear dependence of the equilibrated anelastic strain under constraint on the applied stress was observed, which also implied a linear anelastic strain profile across the sample thickness. Consequently, there was no residual stress upon constraint removal.

In the present work, anelastic relaxation is studied at higher strain than in our prior work, such that the viscosity under

constraint is non-Newtonian, but STZ volume fractions are still small, ≤7.2%. Unlike in the linear regime, this approach allows for an independent determination of the STZ volume and transformation strain for the largest activated STZs.

II. BACKGROUND

Ju et al.[12] obtained time-constant spectra for anelastic relaxation for amorphous $Al_{86.8}Ni_{3.7}Y_{9.5}$, which exhibited a set of distinct peaks. They modeled the behavior with a standard linear solid model (Fig. 1)—a spring in series with several Voigt units, each of which represents one peak and STZ size, and contributes additively to the total strain. Analysis of the data, assuming a transformation shear strain of 0.2,[3,4] revealed that each peak corresponded to an STZ size that comprises a discrete number of Al atoms. A size increment of one atom corresponds to about an order of magnitude larger time constants. Under constraint for 2×10^6 s at a fixed strain, all but the largest and slowest STZs, those comprising $n = 21$ atoms, essentially reach mechanical equilibrium with each other and the elastic matrix and then track the slow evolution of the $n = 21$ STZs. (For longer constraining time, $n = 22$ STZs were also activated.[13]) After constraint removal, each STZ size evolves independently in this model.

In Ref. 12, the shear strain rate due to STZs indexed with the integer m under an applied shear stress, σ, was expressed as[3]

$$\dot{\gamma}_m = 2c_m \gamma_o^c v_G \exp\left(-\frac{\Delta F_m}{kT}\right) \sinh\left(\frac{\sigma \gamma_o^T \Omega_m}{2kT}\right), \quad (1)$$

where $m = 1,\ldots,8$. c_m is the volume fraction occupied by potential m-type STZs, where a potential STZ is an atomic cluster that is capable of shear transformation. γ_o^T is the transformation shear strain, and $\gamma_o^c = [2(4 - 5\nu)/(15(1 - \nu))] \times \gamma_o^T$ is its value under constraint by the surrounding matrix, with ν being Poisson's ratio. v_G is the attempt frequency. Ω_m is the volume of m-type STZs. The product $\gamma_o^T \times \Omega_m$ is the activation volume for a shear transformation, i.e., the conjugate of the stress. k and T have the usual meaning. For small σ values, the hyperbolic sine term can be linearized so that the strain rate is proportional to σ. ΔF_m is the activation free energy for shear transformation of m-type STZs,[14]

$$\Delta F_m = \left[\left(\frac{7 - 5\nu}{30(1 - \nu)} + \frac{2(1 + \nu)}{9(1 - \nu)}\bar{\beta}^2\right) \times \gamma_o^T + \frac{1}{2} \times \frac{\overline{\sigma_{STZ}}}{\mu}\right] \mu \gamma_o^T \Omega_m. \quad (2)$$

$\bar{\beta}^2$ is the dilatancy factor and approximately equal to 1, μ is the shear modulus and expressed as $E_0/[2(1 + \nu)]$, and E_0 is Young's modulus. $\overline{\sigma_{STZ}}$ is the shear resistance of an STZ if it were not embedded in the matrix. The three terms in Eq. (2) correspond, respectively, to the (a) shear strain energy, (b) dilatation strain energy, and (c) shear energy of the STZ if it were not embedded in the matrix.[15] The parameters in Eqs. (1) and (2), their values, and sources are summarized in Table I and the Nomenclature.

In the linear, i.e., Newtonian regime, the product $(\gamma_0^T)^2 \times \Omega_m$ can be determined, but not each factor independently. An estimated value of $\gamma_0^T = 0.2$, based on physical analogs,[3,4] was used to obtain Ω_m, $m = 1,\ldots,8$ in Refs. 12 and 13. These values were spaced by a single atomic volume. Each Ω_m value is associated with an integer multiple of the atomic value of Al: $\Omega_n = n \times \Omega_{Al}$, where $n = 13 + m$. The range of n values, $14 \leq n \leq 21$, is determined by the range of experimental time scales. In order to determine γ_0^T and $\Omega_{n=21}$ independently, it is necessary to perform measurements at higher stress, in the non-Newtonian regime, where Eq. (1) is not linear in σ. Such an approach was reported for large tensile strains, up to 0.08, using strain-rate jumps and assuming a single STZ size.[14] The present work involves anelasticity measurements in the non-Newtonian regime, but in contrast to Ref. 14, we employ a maximum bending strain of 0.0155, with maximum anelastic shear strain of 0.0060, such that the volume fraction occupied by STZs is still small, ≤7.2%. Therefore, STZ properties are obtained for an inherent state, i.e., a local minimum of the energy landscape. While uniaxial geometry offers zero residual stress and far simpler analysis, experiments in bending geometry, not being instrumented, allow for high precision in a wide dynamic range of time, $\sim 10^2$–3.0×10^7 s for the present work. Using the constitutive law [Eq. (1)] for $n = 21$ STZs and zero-bending-moment condition after constraint removal and complete reversal of STZs with $n < 21$, strain data for $Al_{86.8}Ni_{3.7}Y_{9.5}$ are analyzed, accounting for residual stresses. The volume of the largest and slowest STZ size, for a constraining period of 2×10^6 s, $\Omega_{n=21}$, and the transformation shear strain are obtained independently.

III. EXPERIMENTAL DETAILS

Amorphous $Al_{86.8}Ni_{3.7}Y_{9.5}$ (at. %) ribbons, $22\,\mu$m thick and 1 mm wide, were produced by single-wheel melt-spinning using a Cr-coated Cu wheel at a tangential velocity of 40 m/s in vacuum. In previous bend relaxation measurements,[12] samples were constrained by wrapping around mandrels with radii ranging from 0.35 to 0.49 cm, corresponding to equilibrium elastic bending-strain values from 0.00158 to 0.00303 at the surface. To obtain higher bending strain, up to 0.0155, a constraining method was developed for smaller radii, as illustrated in Fig. 2(a): a sample is placed between a mandrel (radius 0.09 or 0.11 cm) and neoprene block. A machined device is used to press the mandrel until the two ends of the sample just touch each other, so that a well-characterized
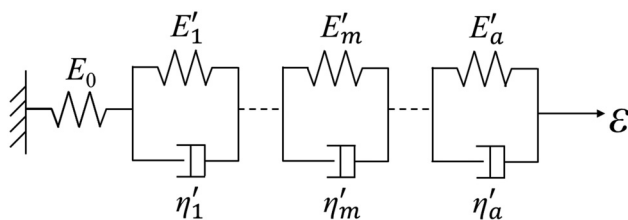

FIG. 1. Schematic illustration of the standard linear solid model employed—a spring with Young's modulus E_0 in series with Voigt units, each of which represents one STZ size. E'_m and η'_m are the effective Young's modulus and effective viscosity, respectively, of m-type STZs, where $m = 1$–8 for the range of time values in the experiment.[12] Reproduced with permission from Ju et al., J. Appl. Phys. **109**, 053522 (2011). Copyright 2011 AIP Publishing LLC.

TABLE I. Parameter definitions in the expression of shear strain rate [Eq. (1)] and activation free energy [Eq. (2)].

Symbol	Physical meaning	Value/Expression
c_m	Volume fraction occupied by potential m-type STZs	Area of corresponding spectrum peak from experiments (Refs. 12 and 13)
m	Index of spectrum peaks	1,…,8 *Note: $n = 13 + m$ = number of atoms in STZ is used as a subscript in Eq. (9) and below it
γ_o^c	Transformation shear strain under constraint by surrounding matrix	$\gamma_o^c = [2(4 - 5\nu)/(15(1 - \nu))] \times \gamma_o^T$
ν_G	Attempt frequency	$10^{13}\,\mathrm{s}^{-1}$ (Ref. 16)
T	Temperature	295.15 K
ΔF_m	Activation barrier associated with m-type STZs	Eq. (2)
σ	Applied shear stress	Expressed in Eqs. (8) and (16)
Ω_m	Volume of m-type STZs	To be determined
$\bar{\beta}^2$	Dilatancy factor	~1 (Ref. 14)
$\overline{\sigma_{STZ}}$	Peak interatomic shear stress between atoms in a regular lattice	$\overline{\sigma_{STZ}}/\mu = 0.025$ (Ref. 17)
ν	Poisson's ratio	0.35 (Ref. 18)
E_0	Young's modulus of the matrix	48.2 GPa (Ref. 19)
μ	Shear modulus of the matrix	$E_0/[2(1 + \nu)]$
γ_o^T	Transformation shear strain in the absence of constraint by the surrounding matrix	To be determined

geometry is obtained. A peephole on the side surface of the machined device is used to observe the two touching ends of the sample during constraining [Fig. 2(b)]. Because of the low modulus of the neoprene, the pressure on the sample is negligible compared to the bending stress. A lubricant was applied between the sample and neoprene to minimize friction. In contrast to the constraining configuration in Ref. 12, in which the entire sample was under constraint, in the present work, only a small section is under constraint, with the two free ends allowing for a reliable determination of the radius of curvature. The detailed constraining geometry is shown in Fig. 3(a). 1 cm long samples were used, and all measurements were performed at room temperature.

As in Ref. 12, samples were constrained for $t_c^{total} = 2 \times 10^6$ s and then relaxed unconstrained for up to 3×10^7 s. The evolution

in the angle between the two ends during unconstrained relaxation [Fig. 3(b)] was recorded with a digital camera and used to determine the curvature of the previously bent section. A stage micrometer was used for calibration, and the optical axis of the camera was aligned perpendicular to the sample stage.

The total constraining strain at a distance y from the sample midplane is

$$\varepsilon_{constr}(y) = y \times (1/R - 1/r_0), \quad (3)$$

where R is the mandrel radius and r_0 is the initial radius of curvature for the sample before constraining. At the end of the constraining period, lasting t_c^{total}, $\varepsilon_{constr}(y)$ includes both an elastic and
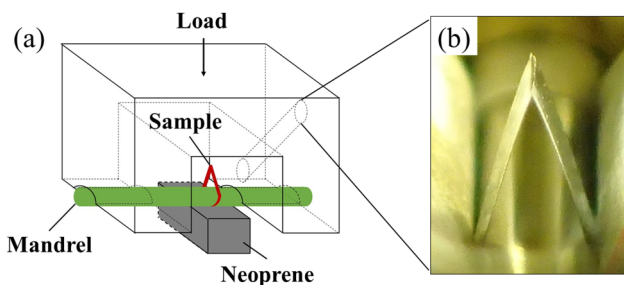

FIG. 2. (a) Schematic illustration of the constraining method—the sample is placed between a mandrel and neoprene block, and a machined device is used to press the mandrel until the two free ends of the sample just touch each other. (b) Photograph showing the two touching ends of a sample under constraint.
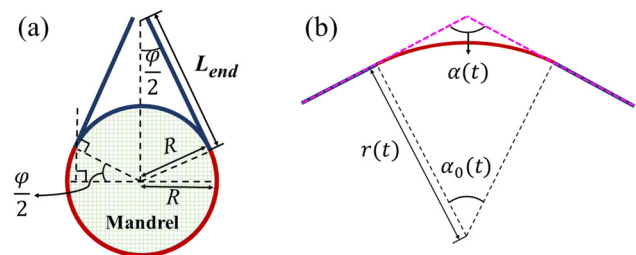

FIG. 3. Sample geometry (a) under constraint and (b) during unconstrained relaxation (not to scale). $\alpha(t)$ is used to determine the evolution of the curvature of the previously bent section during unconstrained relaxation. The length of the constrained section (red) is equal to $(\pi + \varphi) \times (R + d/2)$, where R is the mandrel radius and d is the sample thickness. Dashed lines are fits to the unconstrained ends. The small curvature of the free ends is neglected in these plots.

an anelastic component. We can determine apparent strain values, based on linear variation with y. The apparent elastic strain is

$$\varepsilon_{el,constr}^{app}(y,\ t_c^{total}) = y \times [1/R - 1/r(0)], \tag{4}$$

where $r(t)$ is the radius of curvature of the previously constrained section at time t after constraint removal. The apparent anelastic strain is

$$\varepsilon_{an,constr}^{app}(y, t_c^{total}) = y \times [1/r(0) - 1/r_0]. \tag{5}$$

Note that unlike the elastic strain, the apparent anelastic strain at the end of the constraining period is equal to its value at $t = 0$ after constraint removal, $\varepsilon_{an}^{app}(y, t = 0)$.

Substitution of $r(t)$ for $r(0)$ in Eq. (5) provides the apparent anelastic strain at time t after constraint removal. In the case of Newtonian behavior, when the strain profile across the sample thickness is linear, the expressions for the apparent strains are equal to the actual values. However, in the nonlinear regime, the anelastic strain is superlinear close to the surface. As a result, there is residual stress near each surface in the unconstrained state, with signs opposite of those under constraint. $\varepsilon_{an}^{app}(d/2, t)$, d being the sample thickness, is then lower than the actual anelastic strain at the surface.

While it would be challenging to directly measure the radius of curvature of the small constrained section during unconstrained relaxation, the well-characterized geometry (Fig. 3) allows for a reliable determination of $r(t)$ from the angle between two fit lines to the free ends [dashed lines in Fig. 3(b)]. For different mandrel radii used, the maximum constraining strain ranges from 0.0079 to 0.0155, below the yield point ($\sim$0.02).[20] This was verified by the observation that constraining for a short duration did not lead to permanent deformation. The estimated volume fraction occupied by STZs, based on the anelastic strain, is between 3% and 7.2%, still in the dilute limit.

It was shown in Ref. 12 that the time constant for anelastic recovery of the largest active STZs (consisting of 21 Al atoms) is $\tau_{21} = 1.25 \times 10^7$ s, significantly longer than the total constraining time ($t_c^{total} = 2 \times 10^6$ s). All other τ_i, $i \leq 20$, are smaller than 10^6 s.[12] It follows that all but the $n = 21$ STZs nearly equilibrate by the end of the constraining period. Since nonlinearity affects the kinetics but not the mechanical equilibrium state, it therefore only affects the contribution of $n = 21$ STZs, as these do not equilibrate during the constraining time. In order to isolate this contribution, the apparent anelastic strain after $t = 4 \times 10^6$ s unconstrained relaxation is shown in Fig. 4 as a function of the apparent elastic strain at the end of the constraining period, both computed for the sample surface. The contribution of STZs with $n \leq 20$ atoms to the anelastic strain is negligible at this point ($t = 4 \times 10^6$ s), since these have essentially been fully reversed. The five small-strain data points in Fig. 4, which lie on a straight line, are taken from Ref. 12. Significant deviation from linearity is observed at high strain and stress. The decrease of the anelastic strain due to $n = 21$ STZs from its value at the end of the constraining period, about 27% during unconstrained relaxation for 4×10^6 s, is accounted for in the analysis.
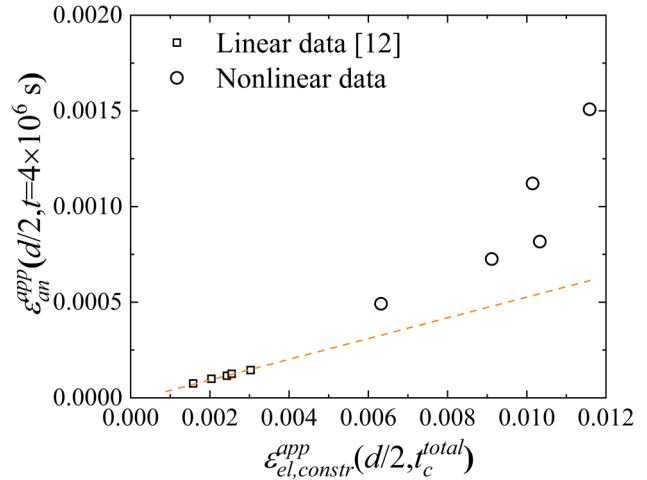

FIG. 4. Apparent anelastic strain after unconstrained relaxation for $t = 4 \times 10^6$ s as a function of the apparent elastic strain at the end of the constraining period for varying constraining radii. Both are computed for the sample surface. Each symbol represents one sample. Deviation from linearity occurs at high strain. The dashed line is a fit to the linear portion.

IV. OVERVIEW OF THE DATA ANALYSIS

"Apparent" strain values below are those determined from curvature by using linear variation across the sample. The term "actual" is used to distinguish strain and stress values from their apparent values. The Nomenclature contains a summary of the notation used below.

1. Applying the condition of zero total bending moment after constraint removal, a relationship between the apparent anelastic strain at the sample surface at $t = 4 \times 10^6$ s after constraint removal, $\varepsilon_{an}^{app}(d/2,\ t = 4 \times 10^6$ s$)$, and the position-dependent anelastic strain due to $n = 21$ STZs at the end of the constraining period, $\varepsilon_{21,constr}(y, t_c^{total})$, is obtained.

2. $\varepsilon_{an}^{app}(d/2, t = 4 \times 10^6$ s$)$ is directly determined from curvature measurements [Eq. (5)]. An expression for $\varepsilon_{21,constr}(y, t_c^{total})$, in terms of the apparent elastic strain at the sample surface at the end of the constraining period, $\varepsilon_{el,constr}^{app}(d/2, t_c^{total})$, is obtained from time integration of the position- and time-dependent macroscopic shear strain rate due to $n = 21$ STZs under constraint, $\dot{\gamma}_{21,constr}(y, t_c)$. Approximations used in this step are detailed below.

3. Substituting the expression for $\varepsilon_{21,constr}(y, t_c^{total})$ into the relationship between $\varepsilon_{an}^{app}(d/2, t = 4 \times 10^6$ s$)$ and $\varepsilon_{21,constr}(y, t_c^{total})$, obtained in step 1 above, yields a fitting equation for $\varepsilon_{an}^{app}(d/2, t = 4 \times 10^6$ s$)$ vs $\varepsilon_{el,constr}^{app}(d/2,\ t_c^{total})$. This equation contains two fitting parameters: the transformation shear strain, γ_0^T, and the volume of $n = 21$ STZs, Ω_{21}.

4. A simultaneous two-parameter fit is performed on all data. The linear portion, which has smaller error, is not fitted as well as with a separate linear fit. A revised two-step fit is performed as follows: first, the linear regime is fitted, which yields the value of $(\gamma_0^T)^2 \times \Omega_{21}$ with small random error. This

value is then used as a constraint for the entire data set to obtain Ω_{21} and γ_0^T.

V. ANALYSIS DETAILS

We first note that for the presently used bending-strain values ≤ 0.0155, nonlinear elastic behavior[21] is likely to be minimal, especially since the long-range elastic field of an STZ dominates ΔF in Eq. (2). Since nonlinearity is observed in Fig. 4, nonlinear kinetics [Eq. (1)] now will be used. After constraint removal, the total bending moment is zero,

$$M(t=0) = \int_{-\frac{d}{2}}^{\frac{d}{2}} [\sigma_{constr}(y, t_c^{total}) - \sigma_u(y, t=0)] \times y \, dy = 0, \quad (6)$$

where $\sigma_{constr}(y, t_c^{total})$ is the applied stress at a distance y from the sample midplane at the end of the constraining period. $\sigma_u(y, t=0)$ is the unloading stress immediately upon constraint removal, which varies linearly across the sample thickness,

$$\sigma_u(y, t=0) = y \times \left[\frac{1}{R} - \frac{1}{r(0)}\right] \times \frac{E_0}{2(1-\nu^2)}. \quad (7)$$

The position-dependent applied stress at the end of the constraining period is

$$\sigma_{constr}(y, t_c^{total}) = [\varepsilon_{constr}(y) - \varepsilon_{an,constr}(y, t_c^{total})] \times \frac{E_0}{2(1-\nu^2)}, \quad (8)$$

where $\varepsilon_{constr}(y)$ is the position-dependent total constraining strain, $y \times [1/R - 1/r_0]$. $\varepsilon_{an,constr}(y, t_c^{total})$ is the sum of the position-dependent anelastic strain due to all active STZ sizes at the end of the constraining period. It consists of contributions: (a) due to STZs comprising n atoms, $\varepsilon_{n,constr}^0(y, t_c^{total})$, $n = 14$–20, which reached mechanical equilibrium during constraining, and (b) due to $n = 21$ STZs, $\varepsilon_{21,constr}(y, t_c^{total})$—these did not reach mechanical equilibrium. Therefore, $\varepsilon_{an,constr}(y, t_c^{total})$ is expressed as

$$\varepsilon_{an,constr}(y, t_c^{total}) = \sum_{n=14}^{20} \varepsilon_{n,constr}^0(y, t_c^{total}) + \varepsilon_{21,constr}(y, t_c^{total})$$
$$= \sum_{n=14}^{20} c_n \times \varepsilon_{el,constr}(y, t_c^{total}) + \varepsilon_{21,constr}(y, t_c^{total}). \quad (9)$$

$\varepsilon_{n,constr}^0(y, t_c^{total})$ equals $c_n \times \varepsilon_{el,constr}(y, t_c^{total})$,[12] where c_n is the volume fraction occupied by potential STZs comprising n atoms, and $\varepsilon_{el,constr}(y, t_c^{total})$ is the position-dependent elastic strain at the end of the constraining period. The values of c_n were obtained in Refs. 12 and 13.

Substituting Eqs. (7)–(9) into Eq. (6), and since $\sigma_{constr}(y, t_c^{total})$ and $\sigma_u(y, t=0)$ are antisymmetric, Eq. (6) immediately after constraint removal becomes

$$\int_0^{\frac{d}{2}} y \times \left[\frac{1}{r(0)} - \frac{1}{r_0}\right] \times y \, dy = \int_0^{\frac{d}{2}} \sum_{n=14}^{20} c_n \times \varepsilon_{el,constr}(y, t_c^{total}) \times y \, dy$$
$$+ \int_0^{\frac{d}{2}} \varepsilon_{21,constr}(y, t_c^{total}) \times y \, dy. \quad (10)$$

After $t = 4 \times 10^6$ s of unconstrained relaxation, the contribution of STZs with $14 \leq n \leq 20$ vanishes, and with $\tau_{21} = 1.25 \times 10^7$ s,[12] the anelastic strain due to $n = 21$ decreases by a factor of 0.73. Consequently, at $t = 4 \times 10^6$ s, the zero-moment condition becomes

$$\boldsymbol{\varepsilon_{an}^{app}}(\boldsymbol{d}/2, \boldsymbol{t} = 4 \times 10^6 \text{ s}) = 0.73 \times \frac{12}{d^2}$$
$$\times \int_0^{\frac{d}{2}} \varepsilon_{21,constr}(y, t_c^{total}) \times y \, dy. \quad (11)$$

The position-dependent anelastic bending strain due to $n = 21$ STZs at the end of the constraining period is

$$\varepsilon_{21,constr}(y, t_c^{total}) = (1-\nu) \times \int_0^{t_c^{total}} \dot{\gamma}_{21,constr}(y, t_c) dt_c, \quad (12)$$

where $(1-\nu)$ is the ratio of bending to shear strain. $\dot{\gamma}_{21,constr}(y, t_c)$ is the actual position-dependent macroscopic shear strain rate due to $n = 21$ STZs after time t_c under constraint. Similar to the total anelastic strain, $\varepsilon_{21,constr}(y, t_c^{total})$ is also equal to the anelastic strain due to $n = 21$ STZs immediately following constraint removal, $\varepsilon_{21}(y, t=0)$. Using Eq. (1) with $n = 21$ corresponding to $m = 8$, the actual position-dependent macroscopic shear strain rate due to $n = 21$ STZs as function of time under constraint is

$$\dot{\gamma}_{21,constr}(y, t_c) = 2c_{21}\gamma_0^c \nu_G \exp\left[-\frac{\Delta F_{21}}{kT}\right] \sinh\left[\frac{\sigma_{constr}(y, t_c)\gamma_0^T \Omega_{21}}{2kT}\right]. \quad (13)$$

The last term in Eq. (2), the shear resistance of an STZ isolated from the matrix, can be neglected,[14] yielding

$$\Delta F_{21} = \left[\frac{(7-5\nu)}{30(1-\nu)} + \frac{2(1+\nu)}{9(1-\nu)} \times \bar{\beta}^2\right] \mu(\gamma_0^T)^2 \Omega_{21}. \quad (14)$$

Substituting Eq. (14) into Eq. (13), the position-dependent strain rate due to $n = 21$ STZs under constraint lasting t_c, $0 \leq t_c \leq t_c^{total}$, becomes

$$\dot{\gamma}_{21,constr}(y, t_c) = 2c_{21}\gamma_0^c \nu_G \times \exp\left[-\left[\frac{(7-5\nu)}{30(1-\nu)} + \frac{2(1+\nu)}{9(1-\nu)} \times \bar{\beta}^2\right] \times \frac{\mu(\gamma_0^T)^2 \Omega_{21}}{kT}\right] \times \sinh\left[\frac{\sigma_{constr}(y, t_c)\gamma_0^T \Omega_{21}}{2kT}\right]. \quad (15)$$

In Eq. (15), the only parameter expected to change significantly with time is the applied stress $\sigma_{constr}(y, t_c)$, since the constraint imposes a fixed total strain. However, since the apparent elastic strain at the sample surface at the end of the constraining period remains within ~25% of its value at the beginning, $\sigma_{constr}(y, t_c)$ will be approximated by the latter value, $\sigma_{constr}(y, t_c) \approx \sigma_{constr}(y, t_c^{total})$. Consequently, $\dot{\gamma}_{21,constr}(y, t_c)$ is approximated as its value at t_c^{total}. This is one of the two approximations used to estimate Eq. (15). The second approximation is based on the apparent elastic strain, as detailed below.

The position-dependent applied stress at the end of the constraining period, $\sigma_{constr}(y, t_c^{total})$, is proportional to the actual position-dependent elastic strain at that point, $\varepsilon_{el,constr}(y, t_c^{total}) = \varepsilon_{constr}(y) - \varepsilon_{an,constr}(y, t_c^{total})$. It will be approximated by its apparent value, Eq. (4), since $\boldsymbol{\varepsilon}_{el,constr}^{app}(\boldsymbol{d/2}, \boldsymbol{t_c^{total}})$ is within ~25% of $\varepsilon_{constr}(d/2)$. Therefore,

$$\sigma_{constr}(y, t_c^{total}) \approx \varepsilon_{el,constr}^{app}(y, t_c^{total}) \times \frac{E_0}{2(1 - \nu^2)}. \qquad (16)$$

Substituting the values of all known parameters, listed above, and Eq. (16) into Eq. (15) yields the approximate position-dependent macroscopic shear strain rate due to $n = 21$ STZs at the end of the constraining period,
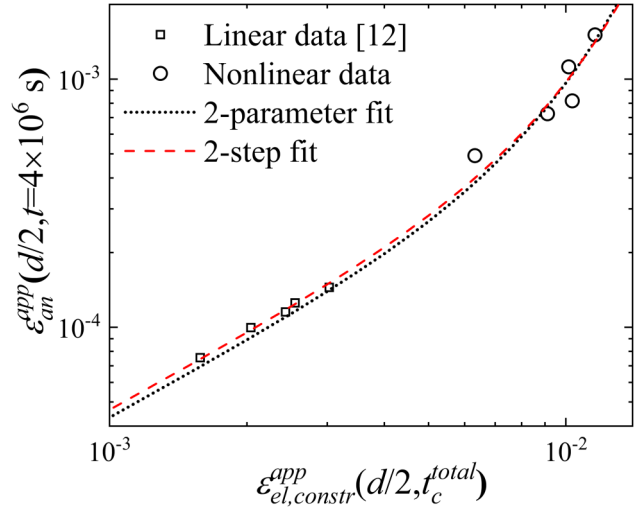

FIG. 5. Data of Fig. 4 on a log-log scale. Comparison between the two-parameter fit (dotted line) and two-step fit (dashed line). The latter yields a better fit for the small-strain data than the former.

$$\dot{\gamma}_{21,constr}^{appr}(y, \ t_c^{total}) = 1.2 \times 10^{12} \times \gamma_0^T \times \exp[-3.20 \times 10^{30} \times (\gamma_0^T)^2 \times \Omega_{21}] \times \ \sinh[3.37 \times 10^{30} \times \varepsilon_{el,constr}^{app}(y, t_c^{total}) \times \gamma_0^T \times \Omega_{21}], \qquad (17)$$

with Ω_{21} in m^3 here and below. Substituting Eq. (17) as an approximation of $\dot{\gamma}_{21,constr}(y, t_c)$ into Eq. (12) yields

$$\varepsilon_{21,constr}(y, t_c^{total}) = 2 \times 10^6 \times 0.65 \times 1.2 \times 10^{12} \times \gamma_0^T \times \exp[-3.20 \times 10^{30} \times (\gamma_0^T)^2 \times \Omega_{21}] \times \ \sinh[3.37 \times 10^{30} \times \varepsilon_{el,constr}^{app}(y, t_c^{total}) \times \gamma_0^T \times \Omega_{21}]. \qquad (18)$$

Substituting Eq. (18) into Eq. (11) results in

$$\boldsymbol{\varepsilon}_{an}^{app}(\boldsymbol{d/2}, \boldsymbol{t} = 4 \times 10^6 \, \boldsymbol{s}) = 3.42 \times 10^{18} \times \gamma_0^T \times \exp[-3.20 \times 10^{30} \times (\gamma_0^T)^2 \times \Omega_{21}] \times \int_0^1 \sinh[3.37 \times 10^{30} \times \boldsymbol{\varepsilon}_{el,constr}^{app}(\boldsymbol{d/2}, \boldsymbol{t_c^{total}}) \times z \times \gamma_0^T \times \Omega_{21}] z dz, \qquad (19)$$

where $z = 2y/d$. Equation (19) is the fitting equation for measured values of $\boldsymbol{\varepsilon}_{an}^{app}(\boldsymbol{d/2}, \boldsymbol{t} = 4 \times 10^6 \, s)$ as a function of $\varepsilon_{el,constr}^{app}(d/2, t_c^{total})$ (Fig. 4), with γ_0^T and Ω_{21} being the fitting parameters. A Taylor series up to the 11th order (six terms) is used as a good approximation of the hyperbolic sine function.

A two-parameter fit is performed on the entire range of data simultaneously, with equal weight to all points. It is shown in Fig. 5, which displays the data of Fig. 4 on logarithmic scales. The fit yields $\gamma_0^T = 0.17$ and $\Omega_{21} = 5.2 \times 10^{-28} \, m^3$ with a R-squared value of 0.982. The fit sensitivity to each γ_0^T and Ω_{21} is determined by fixing one at different values and using the other as a single fitting parameter. This yields estimated random errors in γ_0^T and Ω_{21} of ±3% and ±6%,

respectively. The main approximation has been to express the applied stress that drives anelastic deformation as linearly varying in y and constant in time. An attempt at fit improvement was made by using the resulting strain distribution to update the applied stress and iterate to obtain a revised fit. The iteration yields a very small change in γ_0^T and Ω_{21}. Moreover, it leads to a slightly worse fit of the (low-scatter) linear portion and is not considered useful. We conclude that the scatter of the data limits any further improvement in the two-parameter fit.

In Fig. 5, it is apparent that the two-parameter fit deviates from the linear portion of the data. Since this portion is more reliable, a revised two-step fit is now employed. For the linear regime,

the hyperbolic sine term in Eq. (19) is linearized,

$$\varepsilon_{an}^{app}(d/2, t = 4 \times 10^6 \text{ s}) = 3.84 \times 10^{48} \times (\gamma_0^T)^2 \times \Omega_{21}$$
$$\times \exp[-3.20 \times 10^{30} \times (\gamma_0^T)^2 \times \Omega_{21}]$$
$$\times \varepsilon_{el,constr}^{app}(d/2, t_c^{total}).$$
(20)

Fitting Eq. (20) to the small-strain data yields a slope of 0.0482, which, when substituted into Eq. (20), yields

$$(\gamma_0^T)^2 \times \Omega_{21} = 1.517 \times 10^{-29} \text{ m}^3,$$
(21)

with a random error of only a small fraction of a percent because this term appears in the exponent in Eq. (19). Substituting Eq. (21) into Eq. (19) and fitting the entire range of data yields $\gamma_0^T = 0.18$ and $\Omega_{21} = 4.8 \times 10^{-28} \text{ m}^3$ with random errors of 1.5% and 3%, respectively. Since the error in $(\gamma_0^T)^2 \times \Omega_{21}$ is much smaller, these two errors are strongly correlated. The R-squared value of the fit is 0.982, which equals that for the two-parameter fit.

The implication of these new results, $\gamma_0^T = 0.18$ and $\Omega_{21} = 4.8 \times 10^{-28} \text{ m}^3$ (~29 Al atoms), for Ref. 12 are now discussed. If one assumes $\gamma_0^T = 0.18$ to be independent of STZ size, it can be used to recalculate the results of Ref. 12. While the previous quantized hierarchy still stands, the present numerical values result in a volume increment of $2.08 \times 10^{-29} \text{ m}^3$, in contrast to Ref. 12, in which it was fortuitously close to the volume of an Al atom ($V_{Al} = 1.66 \times 10^{-29} \text{ m}^3$). This possibly highlights the limitation of the model of Fig. 1 and constitutive law of Refs. 12 and 14 [Eq. (1)]. The present results provide a confirmation of the magnitude of γ_0^T, for which an approximate value of 0.2, obtained from physical analogs,[3,4] was used in our prior work.

Interestingly, despite the lower strain and corresponding STZ volume fraction in the present work, the activation volume we obtain, $\gamma_0^T \times \Omega_{21} = 8.6 \times 10^{-29} \text{ m}^3$, is similar to values obtained from creep in $Pd_{80}Si_{20}$,[14] $10.5 \times 10^{-29} \text{ m}^3$, and from viscosity measurements in undercooled melts, 8×10^{-29}–$1.9 \times 10^{-28} \text{ m}^3$.[22] Because of the different assumptions in Ref. 22, its STZ volume values are about a factor of 5 greater than that of the largest STZ in the present work. Reference 22 follows Ref. 23 in equating the transformation strain to the universal macroscopic yield strain observed, 0.036. We suggest that the former is greater than the latter for the following reasons: (a) Physical analogs (Refs. 3 and 4 indicate larger transformation strains, >0.1). (b) This may be explained by the expectation that macroscopic yield involves autocatalytic STZ avalanches, which likely begin at weak spots and for which local strains are higher than the macroscopic strain.[12] This point is further supported by observations of higher yield stress and strain for smaller dimensions.[24] When comparing results, one should note that our data were obtained at room temperature, and larger STZs are expected to become active with increasing temperature.

We further reiterate the distinction between data obtained at low strain, when STZs are isolated, and at higher strain, when back stress is lost and STZ interactions with each other are significant. Following Ref. 14, the latter activated flow state is reached for a total volume fraction of ~40% occupied by STZs, corresponding to

macroscopic permanent or anelastic shear strains >0.033 for our value of γ_o^T. While the present study expands our work into the nonlinear regime, the macroscopic anelastic shear strain is below 0.0060, with corresponding STZ volume fractions that are still small, ≤7.2%. Reported processes such as stress overshoot[25,26] and loss of neighbors[27] occur at far higher strains.

In conclusion, a method of constraining samples in bending geometry with bending strains up to 0.0155 was developed. The anelastic strain rate was nonlinear in the applied stress due to the high value of the latter. Combining the constitutive law and zero-bending-moment condition, the nonlinear regime allows us to determine the transformation shear strain and atomic volume of the largest active STZs independently, which are 0.18 and $4.8 \times 10^{-28} \text{ m}^3$, respectively. The respective random errors, 1.5% and 3%, are small because these parameters appear in the exponent in the constitutive law.

NOMENCLATURE

"Apparent" strain values below are those determined from curvature by assuming linear variation across the sample. The term "actual" is used to distinguish strain and stress values from their apparent values.

c_n	volume fraction of potential STZs comprising n atoms
d	sample thickness
E_0	Young's modulus (=48.2 GPa[19])
$M(t = 0)$	total bending moment immediately after constraint removal [Eq. (6)]
$m = 1,\ldots,8$	index denoting spectrum peaks
$n = 13 + m$	number of atoms an m-type STZ comprises. Used as a subscript in Eq. (9) and below
R	mandrel radius
r_0	initial radius of curvature of the sample before constraint
$r(t)$	radius of curvature of the previously constrained section at time t
T	temperature (=295.15 K)
t	time during unconstrained relaxation after constraint removal
t_c	time under constraint
t_c^{total}	total constraining time, equal to 2×10^6 s
y	distance from sample midplane
z	normalized distance from sample midplane, $2y/d$

Greek

$\bar{\beta}^2$	dilatancy factor (≈ 1[14])
ΔF_m	activation barrier associated with m-type STZs
ΔF_{21}	activation free energy for shear transformation of $n = 21$ STZs

$\varepsilon_{an}^{app}(y, t)$	apparent position-dependent anelastic strain at time t after constraint removal, obtained from curvature by assuming a linear dependence of the anelastic strain on y [Eq. (19)]
$\varepsilon_{an,constr}^{app}(y, t_c^{total})$	apparent position-dependent anelastic strain at the end of the constraining period, obtained from curvature by assuming a linear dependence of the anelastic strain on y [Eq. (5)]. Actual value is defined below
$\varepsilon_{constr}(y)$	position-dependent constraining strain [Eq. (3)]
$\varepsilon_{an,constr}(y, t_c^{total})$	total position-dependent anelastic strain due to all active STZ sizes at the end of the constraining period [Eq. (9)]
$\varepsilon_{el,constr}(y, t_c^{total})$	actual position-dependent elastic strain at the end of the constraining period
$\varepsilon_{el,constr}^{app}(y, t_c^{total})$	apparent position-dependent elastic strain at the end of the constraining period, obtained from curvature by assuming a linear dependence of the elastic strain on y [Eq. (4)]. Actual value is defined below
$\varepsilon_{n,constr}^{0}(y, t_c^{total})$	equilibrium position-dependent anelastic strain due to STZs comprising n atoms ($n = 14$–20) at the end of the constraining period
$\varepsilon_{21,constr}(y, t_c^{total})$	position-dependent anelastic strain due to $n = 21$ STZs, which did not reach mechanical equilibrium, at the end of the constraining period [Eqs. (12) and (18)]
γ_0^c	constrained transformation shear strain, equal to $[2(4 - 5v)/(15(1 - v))] \times \gamma_0^T$
γ_0^T	unconstrained transformation shear strain
$\dot{\gamma}_{21,constr}(y, t_c)$	actual position-dependent macroscopic shear strain rate due to $n = 21$ STZs as a function of time under constraint [Eqs. (13) and (15)]
$\dot{\gamma}_{21,constr}^{appr}(y, t_c^{total})$	position-dependent macroscopic shear strain rate due to $n = 21$ STZs at the end of the constraining period approximated as constant in time [Eq. (17)]
k	Boltzmann constant
μ	shear modulus, equal to $E_0/[2(1 + v)]$
v	Poisson's ratio ($= 0.35$[18])
v_G	attempt frequency ($= 10^{13}$ s^{-1}[16])
Ω_m	volume of m-type STZs
Ω_{21}	volume of STZs comprising $n = 21$ atoms
$\sigma_{constr}(y, t_c^{total})$	position-dependent applied stress at the end of the constraining period [Eq. (8)]
$\sigma_u(y, t = 0)$	position-dependent unloading stress immediately after constraint removal [Eq. (7)]
$\overline{\sigma_{STZ}}$	shear resistance of STZs
$\overline{\sigma_{STZ}}/\mu = 0.025$[17]	
τ_n, $n = 14, \ldots, 21$	time constant for unconstrained anelastic relaxation associated with STZs comprising n atoms

REFERENCES

[1] M. F. Ashby and A. L. Greer, Scr. Mater. **54**, 321 (2006).
[2] H. J. Leamy, H. S. Chen, and T. T. Wang, Metall. Trans. **3**, 699 (1972).
[3] A. S. Argon, Acta Metall. **27**, 47 (1979).
[4] P. Schall, D. A. Weitz, and F. Spaepen, Science **318**, 1895 (2007).
[5] L. Li, E. R. Homer, and C. A. Schuh, Acta Mater. **61**, 3347 (2013).
[6] M. L. Falk and J. S. Langer, Annu. Rev. Condens. Matter Phys. **2**, 353 (2011).
[7] M. L. Falk and J. S. Langer, Phys. Rev. E **57**, 7192 (1998).
[8] C. A. Schuh, T. C. Hufnagel, and U. Ramamurty, Acta Mater. **55**, 4067 (2007).
[9] E. Orowan, in *Proceedings of the First U.S. National Congress of Applied Mechanics* (ASME, 1952), p. 453.
[10] L. J. Dijkstra and R. J. Sladek, JOM **5**, 69 (1953).
[11] C. Zener, *Elasticity and Anelasticity of Metals* (University of Chicago Press, Chicago, 1948).
[12] J. D. Ju, D. Jang, A. Nwankpa, and M. Atzmon, J. Appl. Phys. **109**, 053522 (2011).
[13] M. Atzmon and J. D. Ju, Phys. Rev. E **90**, 042313 (2014).
[14] A. S. Argon and L. T. Shi, Acta Metall. **31**, 499 (1983).
[15] J. D. Eshelby, Proc. R. Soc. A **241**, 376 (1957).
[16] A. S. Nowick and B. S. Berry, *Anelastic Relaxation in Crystalline Solids* (Academic, New York, 1972).
[17] H. Kato, H. Igarashi, and A. Inoue, Mater. Lett. **62**, 1592 (2008).
[18] W. H. Wang, Prog. Mater. Sci. **57**, 487 (2012).
[19] J. M. Freitag, R. G. Koknaev, R. Sabet-Sharghi, M. Koknaeva, and Z. Altounian, J. Appl. Phys. **79**, 3967 (1996).
[20] B. J. Yang, J. H. Yao, J. Zhang, H. W. Yang, J. Q. Wang, and E. Ma, Scr. Mater. **61**, 423 (2009).
[21] J. Das, M. Boström, N. Mattern, Å. Kvick, A. R. Yavari, A. L. Greer, and J. Eckert, Phys. Rev. B **76**, 092203 (2007).
[22] J. Krausser, K. H. Samwer, and A. Zaccone, Proc. Natl. Acad. Sci. **112**, 13762 (2015).
[23] W. L. Johnson and K. Samwer, Phys. Rev. Lett. **95**, 195501 (2005).
[24] S. Nachum and A. L. Greer, J. Alloy Compd. **615**, S98 (2014).
[25] P. De Hey, J. Sietsma, and A. Van den Beukel, Acta Mater. **46**, 5873 (1998).
[26] A. Zaccone, P. Schall, and E. M. Terentjev, Phys. Rev. B **90**, 140203(R) (2014).
[27] M. Laurati, P. Maßhoff, K. J. Mutch, S. U. Egelhaaf, and A. Zaccone, Phys. Rev. Lett. **118**, 018002 (2017).